Astronomy & Astrophysics manuscript no. draft_cor
December 7, 2022
©ESO 2022

arXiv:2212.03216v1 [astro-ph.GA] 6 Dec 2022

The softness diagram for MaNGA star-forming regions: diffuse ionized gas contamination or local HOLMES predominance?

E. Pérez-Montero[1], I. A. Zinchenko[2,3], J. M. Vílchez[1], A. Zurita[4,5], E. Florido[4,5], and B. Pérez-Díaz[1]

[1] Instituto de Astrofísica de Andalucía (CSIC), Apartado 3004, 18080 Granada, Spain
[2] Faculty of Physics, Ludwig-Maximilians-Universität, Scheinerstr. 1, 81679 Munich, Germany
[3] Main Astronomical Observatory, National Academy of Sciences of Ukraine, 27 Akademika Zabolotnoho St., 03680, Kyiv, Ukraine
[4] Dpto. de Física Teórica y del Cosmos, Campus de Fuentenueva, Edificio Mecenas, Universidad de Granada, E18071–Granada, Spain
[5] Instituto Carlos I de Física Teórica y Computacional, Facultad de Ciencias, Universidad de Granada, E18071–Granada, Spain

Received XXX; accepted YYY

ABSTRACT

Aims. We explore the so-called *softness diagram* —whose main function is to provide the hardness of the ionizing radiation in star-forming regions— in order to check whether hot and old low-mass evolved stars (HOLMES) are significant contributors to the ionization within star-forming regions, as suggested by previous MaNGA data analyses.
Methods. We used the code HCm-Teff to derive both the ionization parameter and the equivalent effective temperature (T_*), adopting models of massive stars and planetary nebulae (PNe), and exploring different sets of emission lines in the softness diagram to figure out the main causes of the observed differences in the *softness parameter* in the MaNGA and CHAOS star-forming region samples.
Results. We find that the fraction of regions with a resulting $T_* > 60kK$, which are supposedly ionised by sources harder than massive stars, is considerably larger in the MaNGA (66%) than in the CHAOS (20%) sample when the [S II] $\lambda\lambda$ 6716,6731 Å emission lines are used in the softness diagram. However, the respective fractions of regions in this regime for both samples are considerably reduced (20% in MaNGA and 10% in CHAOS) when the [N II] emission line at λ 6584 Å is used instead. This may indicate that diffuse ionised gas (DIG) contamination in the lower resolution MaNGA data is responsible for artificially increasing the measured T_* as opposed to there being a predominant role of HOLMES in the H II regions.

Key words. Galaxies: abundances – Galaxies: stellar content – Galaxies: star formation

1. Introduction

Optical emission lines have traditionally been used as bright tracers of the properties of the H II regions where they are produced. Among them, collisionally excited lines (CELs), given that they are among the brightest in the optical spectrum, can be calibrated, either empirically or based on models, in order to derive several of the so-called functional parameters that govern the basic physics of the ionized gas, which include the metal content, the excitation, or the hardness of the ionizing source.

Among the different strategies used to comparatively quantify the shape of the incident spectral energy distribution (SED), Vilchez & Pagel (1988) defined the so-called *softness* parameter as

$$\eta = \frac{O^+/O^{2+}}{S^+/S^{2+}} \quad (1)$$

based on the assumption that the quotient of the two defined ionic abundance ratios minimizes the dependence on ionization parameter (i.e., the ratio between the number of hydrogen-ionizing photons and the density of particles, usually denoted as U) and can be derived using only available optical CELs. The parameter is defined in such a way that lower values of η correspond to harder ionizing SEDs. An alternative version of this parameter was also defined that uses corresponding emission line fluxes, though a small dependence on the electron temperature is present in this case:

$$\eta' = \frac{[\mathrm{OII}]\lambda 3727/[\mathrm{OIII}]\lambda\lambda 4959,5007}{[\mathrm{SII}]\lambda\lambda 6717,6731/[\mathrm{SIII}]\lambda\lambda 9059,9532}. \quad (2)$$

A different model-based approach was proposed by Pérez-Montero et al. (2019), given that using only the involved emission-line ratios in a two-dimensional plot known as the *softness diagram* helps to separate the dependence of these ratios on metallicity, log U, and the hardness of the incident SED. In addition, when comparing the observed ratios with the results from photoionization models with a SED scalable in terms of an equivalent effective temperature (e.g., massive single stars or blackbody), the diagram can provide a quantification of this hardness.

Although this methodology can be successfully used in certain H II regions in disk galaxies, it does not allow proper coverage of the space of observed emission line fluxes in certain regions observed with IFS, such as in MaNGA (Kumari et al. 2021), as this presents lower η' values, on average, and therefore a harder incident field of radiation.

Several authors (e.g., Mannucci et al. 2021) have recently studied the average differences observed between some of the emission-line ratios involved in η', such as [S II]/[S III], in samples of H II regions observed using long-slit spectrophotometry, such as CHAOS (Berg et al. 2015), in relation to other samples

based on IFS, such as MaNGA. According to these authors, the lower observed [S II]/[S III] ratios in CHAOS could be a consequence of incomplete coverage of the ionization structure, but this is difficult to reconcile with the fact that the [O II]/[O III] is higher in the same regions as compared to IFS data and that photoionization models, which provide integrated emission-line fluxes, do not predict [S II] fluxes as high as those observed when only massive stars are considered.

As opposed to the study of a single low- to high-ionization emission-line flux ratio, the analysis of the softness diagram, could in turn point to the predominance of very hard ionizing sources, such as the hot low-mass evolved stars (HOLMES; Flores-Fajardo et al. 2011). The hard SED from HOLMES can significantly contribute to the [O III] and [S II] emission (e.g., Belfiore et al. 2022) and, as shown by Kumari et al. (2021), models with an older stellar population like those calculated in Morisset et al. (2016) could in principle cover the region with very low η' values observed for star-forming regions detected in MANGA data.

The application of a method such as HCm-Teff, a bayesian-like code that can provide solutions comparing the predictions from models with the observational positions of data in the softness diagram, can shed light on this question by incorporating SEDs compatible with HOLMES and allowing the study of alternative emission lines in order to explore the observed differences between long-slit- and IFS-based samples.

In this work, we compiled emission-line data from both MaNGA and CHAOS, studying their position in the softness diagram, and comparing them with the results from models and the corresponding calculations made by HCm-Teff. This study will allow us to disentangle the possible role of HOLMES and/or the contribution of the diffuse ionized gas (DIG) in the observations, quantifying the corresponding effect in the results.

The paper is organized as follows. In Section 2 we describe the observational samples of compiled optical emission lines. In Section 3 we provide details of the computed photoionization models to be compared with the observations, and of the last version of the code HCm-Teff. In Section 4 we present our results and then discuss them, and finally in Section 5 we summarize our findings and provide conclusions.

2. Data samples

2.1. The MaNGA sample

The Mapping Nearby Galaxies at Apache Point Observatory (MaNGA; Bundy et al. 2015) is part of the Sloan Digital Sky Survey IV (SDSS IV; Blanton et al. 2017). For this work, we used data release 17 (DR17, Abdurro'uf et al. 2022), from which we selected 2124 galaxies in the redshift range $0.0005 < z < 0.0845$. We use individual spaxels whose size is significantly smaller than that of the point spread function (PSF) in the MaNGA datacubes. The spatial resolution of these cubes has a median full width at half maximum (FWHM) of 2.54 arcsec (Law et al. 2016). As our sample has a median z of 0.024, this corresponds to an average spatial resolution of 1.2 kpc.

We collected emission-line fluxes of [O II] λ3727 Å, [O III] $\lambda\lambda$4959,5007 Å, [N II] λ6584 Å, [S II] $\lambda\lambda$6717,6731 Å, [Ar III] λ7135 Å, and [S III] $\lambda\lambda$9069,9532 Å, and obtained a signal-to-noise ratio (S/N) of at least 10 in all selected lines. This implies a total of 201 735 spectra. To obtain the emission line fluxes, we used the STARLIGHT code (Cid Fernandes et al. 2005; Mateus et al. 2006; Asari et al. 2007) to subtract the stellar background and the ELF3D code to fit the emission lines. Details about the processing can be found in Zinchenko et al. (2016, 2021). The line fluxes were corrected for interstellar reddening using the analytical approximation of the Whitford interstellar reddening law (Izotov et al. 1994), assuming the Balmer line ratio of $H\alpha/H\beta = 2.86$. When the measured value of $H\alpha/H\beta$ is less than 2.86, the reddening is set to zero.

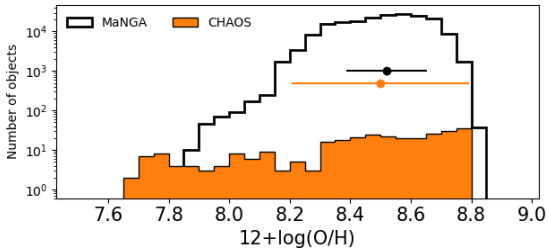


Fig. 1. Distribution of the total oxygen abundances derived for the two studied samples as obtained using HCm.

2.2. The CHAOS sample

The CHAOS (CHemical Abundances Of Spirals) project has been collecting data to build a large database of high-quality, 1" width, long-slit optical spectra of the H II regions of nearby spiral galaxies using the Multi-Object Double Spectrographs (MODS) on the Large Binocular Telescope (LBT).

We compiled data from the literature corresponding to the relative reddening-corrected emission-line fluxes necessary to build the various versions of the softness diagrams studied in this work. In particular, we used data for NGC 628 (Berg et al. 2015), NGC 2403 (Rogers et al. 2021), NGC 3184 (Berg et al. 2020), NGC 5194 (Croxall et al. 2015), and NGC 5457 (Croxall et al. 2016). We used the relative to hb emission line fluxes of these lines as reddening corrected by the corresponding authors, but we checked that these corrections lead to results that are compatible, within the errors, with those obtained with the same fluxes corrected for reddening with the assumptions used for the MaNGA data previously described.

3. Description of the models and the HCm-Teff code

We used photoionization models to interpret the position of the observed regions in the softness diagram, and to provide predictions of the emission-line fluxes under different assumed conditions in order to derive the equivalent effective temperature (T_*) and the ionization parameter (U) with the HII-CHI-mistry-Teff code (HCm-Teff[1]. All photoionization models used in this work were calculated using the code Cloudy v. 17 (Ferland et al. 2017) and are described in Pérez-Montero et al. (2019). In addition to the SEDs described in this latter work, corresponding to O-stars from WM-Basic (Pauldrach et al. 2001) in the T_* range from 30-60 kK, we incorporated SEDs from central stars of planetary nebulae (PNe) from Rauch (2003) in the range 80-120 kK to cover the T_* range that is supposed to be reached by HOLMES. All models were calculated assuming both spherical and plane-parallel geometry, also covering the range of log U from -4.0 to -1.5, and for metallicities as scaled from the total oxygen abundance 12+log(O/H) from 7.1 and 8.9. The remaining chemical species assumed as input in the models were scaled to the solar proportions as given by Asplund et al. (2009), except for N,

[1] All versions of HCm can be retrieved in the public site \protecthttp://www.iaa.csic.es/~epm/HII-CHI-mistry.html

which was scaled to the empirical law given in Pérez-Montero et al. (2014) (i.e., a constant N/O owing to a mostly primary production of N, and increasing N/O at larger Z when secondary N production begins to be important). All models also consider a standard dust-to-gas mass ratio and a filling factor of 0.1.

The HCm-Teff code was presented and described in Pérez-Montero et al. (2019). It can be used to derive both T_* and log U by performing a bayesian-like comparison between the predictions from the grids of models and some specific emission-line flux ratios, involving reddening-corrected high and low-excitation emission-lines (e.g., [O II]/[O III], [S II]/[S III]).

It is known that the ratios of low- to high-excitation lines can be affected by the geometry of the gas if a fraction of ionizing photons escape from the nebula. The code can also be used to derive this fraction using alternative grids of matter-bounded geometry models with Bpass (Eldridge et al. 2017) cluster atmospheres at different stellar metallicities (Pérez-Montero et al. 2020). However, for this work we only consider models assuming a radiation-bounded geometry.

Briefly, the code calculates T_* and log U as the average of the resulting χ^2-weighted distributions of all the results of the models of the grids, with χ^2 values being calculated as the quadratic differences between the observed and predicted corresponding emission-line ratios. The code also provides errors on the derived values, which are calculated as the quadratic addition of the standard deviations of the same distributions and the dispersion resulting from a Monte Carlo iteration perturbing the nominal emission-line flux values with the provided observational errors.

As shown by different authors (e.g., Morisset 2004; Pérez-Montero & Vílchez 2009), metallicity plays an important role in the position of the regions in the softness diagram, and so the code firstly interpolates the grids to the O/H value given as input in each region. If no O/H is given, the code finds a solution using the grid of models for all O/H values, which subsequently leads to a larger uncertainty, as discussed in Pérez-Montero et al. (2019). The error in the input oxygen abundance is also taken by the code for its consideration in the error of the results in the Monte Carlo iteration.

Then, in order to better constrain the solutions for T_* and U, we derived the oxygen abundance values in both samples using HCm version 5.22 (Pérez-Montero et al. 2014) and the models calculated with Popstar (Mollá et al. 2009) SEDs, and using as input all the collected emission lines mentioned above. Also, to this end we also used the auroral [O III] λ 4363 Å line in the case of a subsample of CHAOS (i.e., 134 H II regions). As discussed in several works (Pérez-Montero et al. 2014, 2016), this method is totally consistent with the direct method, even in the absence of any auroral line, although with a larger uncertainty (e.g., the mean O/H error in CHAOS for the H II regions with [O III] λ 4363 Å is 0.11 dex, while for the rest it is 0.18 dex). When no auroral line is given as an input, the code considers the empirical relation between O/H and excitation. In a similar way, when N/O cannot be directly calculated, the code assumes an empirical law between O/H and N/O in order to derive metallicities. For these cases, we used the laws derived by Pérez-Montero et al. (2014) for star-forming regions.

In the case of MaNGA, we did not use [S II] lines as input for HCm in order to derive chemical abundances, as the N2S2 ratio leads to very low values of N/O as compared to those obtained with N2O2, as discussed by Zinchenko et al. (2021). In the case of CHAOS, a certain contamination from iron emission to the [O III] λ 4363 Å has been reported in some galaxies of this sample (Rogers et al. 2021), but we checked that the effect of this difference in the final obtained oxygen abundances is not larger than the obtained errors and, in any case, does not lead to noticeably different results for our derived T_* and U. In Figure 1, we show the distribution of the obtained oxygen abundances in both samples. Although MaNGA spread over larger metallicities, which is consistent with the fact that this sample includes more galaxies, covering a wider range of properties, both distributions present an identical median value of 8.52 (± 0.13 for MaNGA, and ± 0.25 for CHAOS), which is around $0.7 \cdot Z_\odot$.

4. Results and discussion

4.1. Softness diagram based on [O II]/[O III] and [S II]/[S III]

The left panel of Figure 2 shows the softness diagram using the emission-line ratios [O II]/[O III] versus [S II]/[S III] for the selected regions in CHAOS and MaNGA as compared with the results from photoionization models with spherical geometry at two different metallicity values (i.e., 12+log(O/H) = 8.0 and 8.9). The same figure also shows some sequences of models calculated assuming plane-parallel geometry at the higher O/H value, which are used here to explore the effect of the assumed geometry on the results. The represented models have T_* values in the range of 30-60 kK (i.e., using WM-Basic O star atmospheres) and 80-120 kK (using planetary nebulae (PNe) non-local thermodynamic equilibrium (non-LTE) stellar atmospheres), and they also cover a wide range in log U going from -4.0 to -1.5, which in the plot corresponds to the sequences going from the upper-right part to the lower-left regions of the plot, respectively.

We note that an important fraction of the two samples lies in a region of the diagram that could only be explained by invoking effective temperatures higher than the maximum value reachable by O stars (i.e., 60 kK). Moreover, a fraction of the regions could have T_* values larger than the maximum predicted by PNe even for the largest possible metallicity assumed in the models. Although the fraction of points covered by the models with massive stars is slightly higher for spherical than for plane-parallel geometry, the discrepancy for most of the sample not covered by these models cannot be attributed to the assumed geometry. Nonetheless, for the sake of simplicity, in what follows we only focus on the results from models assuming spherical geometry, as this assumption is more realistic. In any case, this fraction of regions that would require very high T_* according to this softness diagram is considerably smaller for CHAOS than for MaNGA.

In order to quantify this behavior, we used the code HCm-Teff for both the selected MaNGA and CHAOS samples to derive T_* and U. The code accepts different emission lines, but we only introduced those involved in the softness diagram shown in the left panel of Figure 2 (i.e., [O II], [O III], [S II] and [S III]) as input in a first step. As an additional input, we introduced the derived metallicity for each point. Although only two values of metallicity are represented in left panel of Figure 2, all possible values are considered by the code in order to cover the entire range and to properly interpolate to the corresponding derived O/H in each point.

The right panel of Figure 2 shows the distributions of the obtained values in both samples when a spherical geometry is assumed. When a plane-parallel geometry is assumed, the derived T_* and log U values are, on average, higher by 2kK and 0.01 dex, respectively. These discrepancies are lower than the grid step for the corresponding values, meaning that the geometry assumed in the model has, on average, no significant impact on our results.

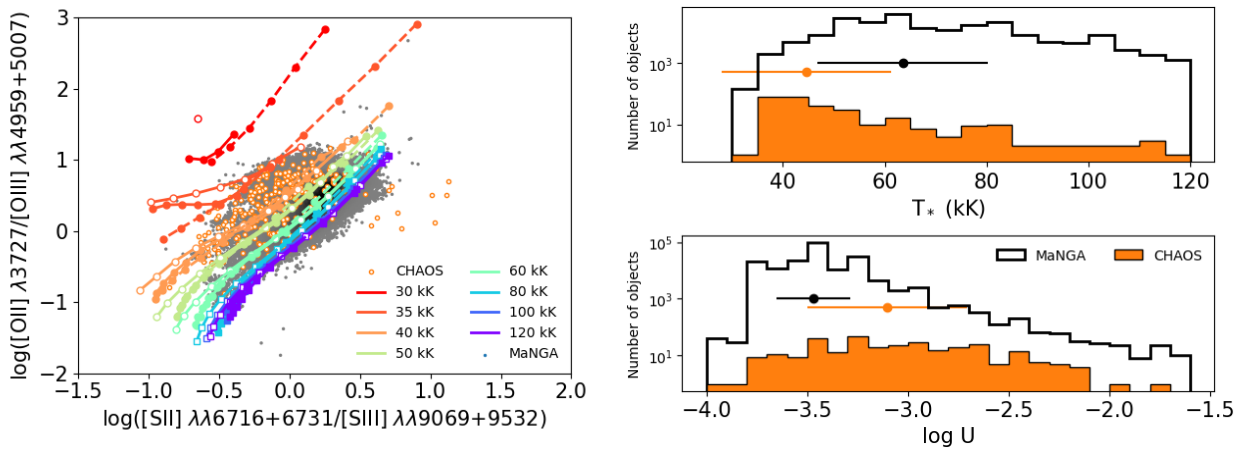


Fig. 2. Softness diagram and effective temperature and ionization parameter distributions in our samples. Left panel: Softness diagram representing [O II]/[O III] vs [S II]/[S III] for the selected regions in CHAOS and MaNGA as compared with different model sequences calculated using WM-Basic atmospheres for T_* between 30 and 60 kK (represented with circles), and Rauch for T_* between 80 and 120 kK (represented with squares). Solid lines represent models with 12+log(O/H) = 8.9, and dashed lines 12+log(O/H) = 8.0. Filled symbols represent models calculated assuming spherical geometry while empty symbols represent models with plane-parallel geometry (only for O/H = 8.9 in this case). Right panel: Distributions of the derived properties using HCm-Teff (upper panel: T_*, lower panel: log U) using as input the metallicity and the emission line-ratios represented in the left panel. The empty histograms represent the MaNGA sample and the orange ones the CHAOS sample. The median and standard deviations are represented in all panels in the same colors.

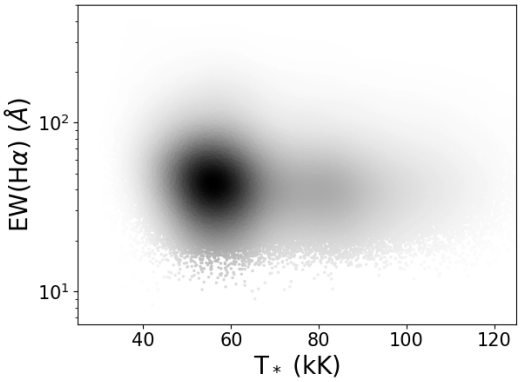


Fig. 3. Relation between T_* as derived from HCm-Teff and the equivalent width of Hα in Å in the MaNGA sample

Consistently with the position of the regions in both samples in the softness diagram, MaNGA presents a larger median T_* (64 ± 17 kK) than in CHAOS (45 ± 16 kK). The mean associated error for each derivation is around 9 kK for MaNGA and 5 kK for CHAOS. This difference is due to the fact that the resolution of the grid of models is lower for higher T_*. In fact, a significantly larger fraction of the regions in MaNGA could have $T_* > 60$ kK than in CHAOS (66% and 20%, respectively).

A similar result is obtained for the distribution of derived log U values, which is shown in the lower right panel of Figure 2, with a median value significantly lower for MaNGA (-3.47 ± 0.18) than for CHAOS (-3.10 ± 0.40), in agreement with the fact that [S II]/[S III] is significantly higher in the first sample. The typical error in the derivation of log$U$ is 0.06 dex for MaNGA and 0.10 dex for CHAOS.

Given the results obtained by HCm-Teff using these specific emission lines, we can explore to what extent it is reasonable to expect that a large fraction of the regions observed in MaNGA have T_* values dominated by a predominant population of HOLMES. This can be done by deciphering whether or not there is any correlation between the derived T_* values and other observational spectral features indicative of the average evolutionary status of the ionizing stellar population. For instance, the relation between the derived T_* values and the equivalent width of Hα measured within the region apertures in the MaNGA survey selected for this work does not show a clear correlation (i.e., the Spearman correlation coefficient, ρ_S is -0.04), as can be seen in Figure 3. Moreover, regions with a derived $T_* > 60$ kK do not present a noticeably lower EW(Hα) on average (i.e., 79 Å) than those with a lower T_* value (85 Å).

Therefore, even taking into account the fact that the continuum signal has a large contribution from the underlying disk stellar population in the IFS data, which can contain HOLMES (e.g., Zhang et al. 2017), no evidence is found to support the hypothesis that certain regions have larger T_* values due to the increased presence of more evolved, harder stellar populations compared to young ionizing ones.

4.2. The softness diagram based on [O II]/[O III] and [S II]/[Ar III]

Among the possible sources of uncertainty in the results obtained using the softness diagram, we can explore the use of [S III] lines, whose atomic coefficients have traditionally shown some known discrepancies with results from photoionization models (e.g., Diaz et al. 1991; Badnell et al. 2015). In addition, [S III] line fluxes can have large uncertainties due to the presence of absorption bands in the spectral range where the lines at λ 9069 and 9532 Å are measured (Diaz et al. 1985).

As an alternative to [S III] lines, we can use the [Ar III] λ 7135 Å line, given the similarity of the ionization potentials of S^+ and Ar^+ and that S and Ar are α-elements that are unaffected by dust depletion. Figure 4 shows the relation between the reddening-corrected emission-line fluxes of [S III] $\lambda\lambda$ 9069+9532 Å and [Ar III] λ 7135 Å, relative to Hβ, for the selected regions in MaNGA. As expected from the fact that these lines trace the same excitation region, the correlation is clear, although the correlation coefficient is moderate (i.e., ρ_S = 0.49). The sequences of photoionization models shown in the same panel indicate that

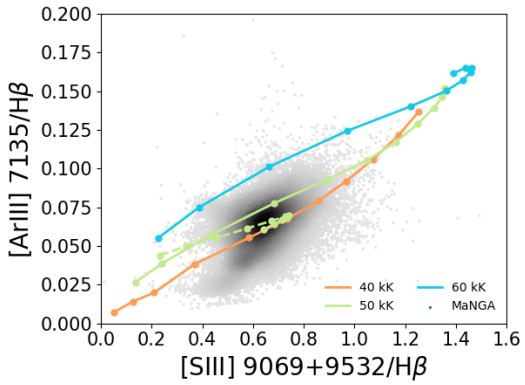


Fig. 4. Relation between the reddening-corrected relative-to-Hβ flux of [S III] $\lambda\lambda$ 9069+9532 Å and [Ar III] λ 7135 Å in the MaNGA sample. Some model sequences for different values of T_* (40 kK in red, 50 kK in green, and 60 kK in blue) and 12+log(O/H) = 8.9 (solid lines) and 8.0 (dashed line) are included.

the observational scatter is not owing to the U variation (i.e., in each sequence varying from log U = -4.0 to -1.5, ρ_S is always higher than 0.99), but additional dependences on T_* and O/H exist. In addition, given the larger wavelength baseline of the [S III] lines in relation to that of their closer HI recombination line, the derived flux of the former can be more affected by the uncertainty in the reddening correction or the presence of telluric emission. Therefore, we can replace the [S III] lines in the corresponding softness diagram and investigate the effect of this replacement on the results.

The left panel of Figure 5 shows the new softness diagram with the emission-line ratio [S II]/[S III] replaced with [S II]/[Ar III]. We first note that the number of regions for which this ratio can be measured with an S/N of at least 10 is significantly smaller for MaNGA (i.e., 32 602 regions), given that the [Ar III] line is weaker than [S III]. In any case, the behavior observed in the previous diagram, namely the large fraction of regions with η' values compatible with the ionization from sources hotter than O stars, is even more pronounced for both samples.

The right panel of Figure 5 shows the corresponding distributions of the resulting T_* and log U from HCM-TEFF when we use the emission lines shown in the softness diagram of Figure 5 as input (i.e., [O II], [O III], [S II] and [Ar III]). The results agree with what can be seen in the softness diagram, as larger fractions of the regions both in MaNGA and CHAOS present T_* larger than 60 kK (i.e., 90% and 54%, respectively). The corresponding median values of the derived T_* also significantly increase for both samples in relation to the previous case, with values of 78 ± 12 kK for MaNGA and 61 ± 12 kK for CHAOS, though they remain compatible within the errors.

On the other hand, contrary to T_*, the differences in the resulting log U distribution are smaller, even though the mean log U in MaNGA (-3.41 ± 0.10) is still lower than in CHAOS (i.e., -3.31 ± 0.21), albeit compatible within the errors. These numbers indicate, on one hand, that the two samples still behave in a different manner when this set of lines is used to derive both T_* and U. On the other hand, as opposed to the results obtained when the [S III] lines are used, the results from this softness diagram —which implies an even larger fraction of regions that are supposedly ionized by HOLMES— cannot be interpreted as due to the use of the [S III] emission line.

4.3. Replacing [S II] with [N II] in the softness diagrams

Another factor that may account for the very high values of the emission-line ratio [S II]/[S III] in the softness diagram is the background DIG contribution to the integrated star-forming region fluxes (e.g., Zurita et al. 2000; Haffner et al. 2009). Given the larger spatial aperture in surveys like MaNGA, which is based on IFS, as compared with CHAOS, this contribution is expected to be greater. Indeed, [S II] emission (relative to Hα) is known to be enhanced in the DIG with respect to the H II regions (Reynolds 1985; Domgorgen & Mathis 1994; Galarza et al. 1999).

Therefore, we investigated the role of this emission line in the softness diagram by replacing this line with another strong low-excitation line, namely [N II] λ 6583 Å. This line can also be contaminated by DIG emission, although to a lesser extent because of the higher ionization potential of N^+ than that of S^+ (e.g., Blanc et al. 2009), and can also be used to trace both the excitation and the shape of the SED in this diagram.

The left panel of Figure 6 shows this new diagram, where [S II] in replaced with [N II] both in the models and the data. Contrary to the previous case with [Ar III], the number of regions in MaNGA for which we can build this diagram is again higher, as this line is bright and easily measurable in most of the regions. As can also be seen, contrary to the previously shown diagrams based on the [S II] lines, no clear difference is observed between the two samples and, in addition, only a small fraction of them apparently lie in the region of the PNe models (i.e., with T_* > 60 kK, supposedly ionized by HOLMES). Although the model sequences for different values of T_* apparently present a larger dependence on metallicity (and therefore on N/O) in this new diagram, the fraction of regions with T_* > 60 kK for both samples does not present a mean total oxygen abundance that is larger within the errors (i.e., 12+log(O/H) = 8.58) than the rest of regions, and, in any case, the O/H values of all the regions are well covered by the grid of models.

As in previous subsections, in the right panel of Figure 6 we show the distributions of T_* and log U calculated by HCM-TEFF using only the corresponding metallicities and the emission lines involved in the softness diagram of Figure 6 as input (i.e., [O II], [O III], [N II] and [S III]). In this case, the replacement of [S II] with [N II] leads to a substantial difference in the results, as the number of regions with a resulting T_* > 60 kK is drastically reduced in both samples (i.e., 20% in MaNGA and 10% in CHAOS). Consistently, the median T_* derived from HCM-TEFF in MaNGA (50 ± 11 kK) and CHAOS (42 ± 8kK) are much more similar, both lying in the regime expected for massive young stars.

Regarding log U, we also find differences in relation to the diagrams based on [S II], as both median values in MaNGA (-2.95 ± 0.31) and in CHAOS (-2.62 ± 0.37) are significantly higher than in previous cases. Although the fraction of regions with T_* values that are consistent with ionization from objects harder than massive stars is much lower when using [N II], it is pertinent to question the extent to which the fractions of star-forming regions in both MaNGA and CHAOS with an effective T_* > 60 kK can be genuinely ionized by a predominant population of HOLMES in the studied regions. In this way, taking EW(Hα) again as a proxy for the mean age of the underlying stellar population, its average is almost identical in the total sample (83 Å) to that in those regions with T_* > 60 kK (i.e., 80 Å) when [N II] is used, and so the very high T_* found in this subsample does not seem to be caused by a real ionization from HOLMES in these regions. On the other hand, given that [N II]

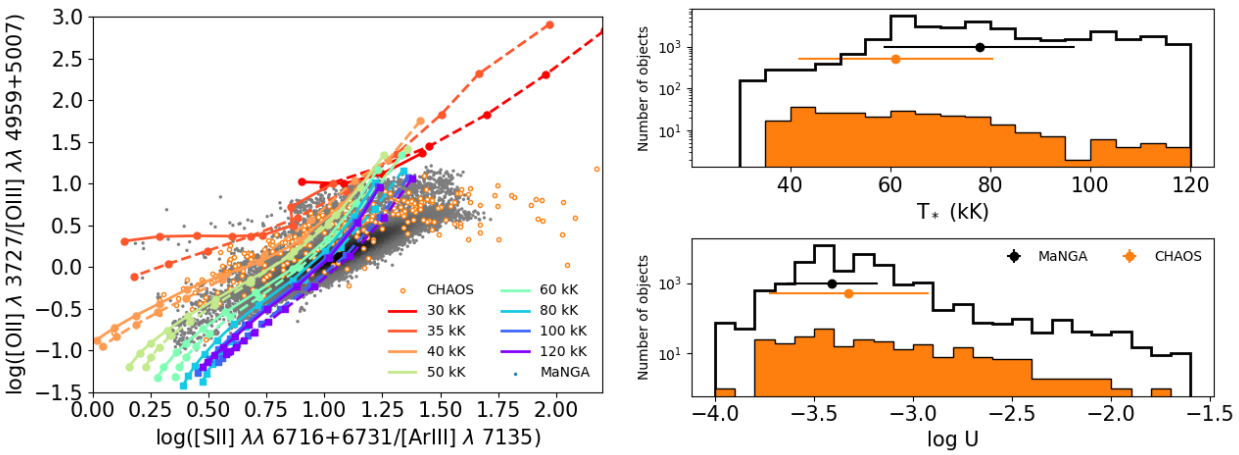


Fig. 5. Same as figure 2 but for [O II]/[O III] vs [S II]/[Ar III], but only for models with spherical geometry.

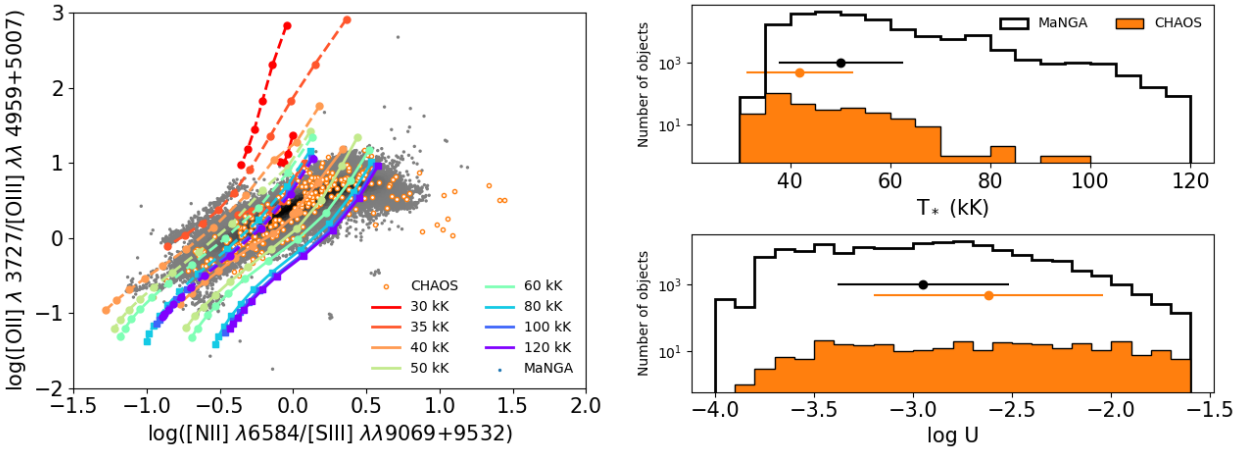


Fig. 6. Same as figure 2 but for [O II]/[O III] vs [N II]/[S III] and only for models with spherical geometry.

can also be contaminated by background DIG emission (e.g., Poetrodjojo et al. 2019), and the higher T_* and lower U values still found in MaNGA in relation to CHAOS, a certain DIG contribution could be responsible for these fractions, even using the [N II] line.

In any case, these results may indicate —assuming that [S II] emission is more contaminated by DIG than [N II]— that a large fraction of the regions in MaNGA is affected by this contribution from the background. This does not exclude HOLMES as contributors to the ionization of the background DIG emission included in the MaNGa spaxels, but would indicate that HOLMES are not the dominant source of ionization in the regions of the MaNGA sample, as suggested by previous work (e.g., Kumari et al. 2021). Therefore, the derived T_* values obtained using certain low-excitation emission lines in low-resolution IFS surveys are possibly not representative of the H II regions covered by large apertures.

This result is consistent with the very different N/O ratios derived in MaNGA by Zinchenko et al. (2021) when using the N2O2 or the N2S2 emission-line ratios, which are much lower in the second case, as a consequence of a possible stronger DIG contamination of [S II] of the H II region fluxes.

5. Summary and conclusions

Using different versions of the softness diagram, involving different ratios of low- to high-excitation emission lines, we investigated the different behavior in this diagram of the observational samples MaNGA and CHAOS. The direct comparison of the observations in the diagram of [O II]/[O III] versus [S II]/[S III] with sequences of photoionization models of single O stars and PNe reveals that most of the regions in MaNGA have $T_* > 60$ kK, which is not true for CHAOS. As this is the maximum considered T_* value in the models for massive stars, this could be indicative that the MaNGA regions are predominantly ionized by HOLMES, as suggested by Kumari et al. (2021). This is in agreement with the results from the code HCm-Teff; when this code translates the positions in this latter diagram into equivalent values for T_* and log U, the corresponding average values and the fraction of star-forming regions with T_* larger than the maximum O star value are found to be much higher for MaNGA than for CHAOS.

This result cannot be associated with any problem related to the [S III] lines at $\lambda\lambda$ 9069,9532 Å (i.e., atomic coefficients, continuum absorption, or telluric contamination), as it is reproduced when these lines are replaced with [Ar III] at λ 7135 Å, which traces a similar excitation zone.

However, when [S II] is replaced with [N II] in the softness diagram, which is less affected by background DIG, both the me-

dian obtained T_* and the fraction of star-forming regions with a value larger than 60 kK are significantly reduced in both samples.

Our results suggest that the DIG contamination may significantly affect the results from this diagram when it is built using [S II], and that local HOLMES are not the predominant source shaping the hardness of the ionizing radiation in the star-forming regions, even in those observed with low spatial resolution, such as in MaNGA. In any case, the true nature of DIG and its contribution to the integrated spectra are still far from clear, as it is also produced by HOLMES. Also, the lack of correlation between the derived T_* with EW(Hα), which also depends on DIG emission (e.g., Lacerda et al. 2018), may indicate that the artificially increased T_* values obtained when certain low-excitation lines are used in low-spatial-resolution data are the product of a combination of emission lines with a different spatial origin rather than the consequence of a characteristic ionizing stellar population.

Acknowledgements. This work has been partly funded by projects Estallidos7 PID2019-107408GB-C44 (Spanish Ministerio de Ciencia e Innovacion), and the Junta de Andalucía for grant P18-FR-2664. We also acknowledge financial support from the State Agency for Research of the Spanish MCIU through the "Center of Excellence Severo Ochoa" award to the Instituto de Astrofísica de Andalucía (SEV-2017-0709). AZ and EF acknowledge support from projects PID2020-114414GB-100 and PID2020-113689GB-I00 financed by MCIN/AEI/10.13039/501100011033, from projects P20-00334 and FQM108, financed by the Junta de Andalucí a, and from FEDER/Junta de Andalucí a-Consejerí a de Transformación Económica, Industria, Conocimiento y Universidades/Proyecto A-FQM-510-UGR20. EPM also acknowledges the assistance from his guide dog Rocko without whose daily help this work would have been much more difficult.

References

Abdurro'uf, Accetta, K., Aerts, C., et al. 2022, ApJS, 259, 35
Asari, N. V., Cid Fernandes, R., Stasińska, G., et al. 2007, MNRAS, 381, 263
Asplund, M., Grevesse, N., Sauval, A. J., & Scott, P. 2009, ARA&A, 47, 481
Badnell, N. R., Ferland, G. J., Gorczyca, T. W., Nikolić, D., & Wagle, G. A. 2015, ApJ, 804, 100
Belfiore, F., Santoro, F., Groves, B., et al. 2022, A&A, 659, A26
Berg, D. A., Pogge, R. W., Skillman, E. D., et al. 2020, ApJ, 893, 96
Berg, D. A., Skillman, E. D., Croxall, K. V., et al. 2015, ApJ, 806, 16
Blanc, G. A., Heiderman, A., Gebhardt, K., Evans, Neal J., I., & Adams, J. 2009, ApJ, 704, 842
Blanton, M. R., Bershady, M. A., Abolfathi, B., et al. 2017, AJ, 154, 28
Bundy, K., Bershady, M. A., Law, D. R., et al. 2015, ApJ, 798, 7
Cid Fernandes, R., Mateus, A., Sodré, L., Stasińska, G., & Gomes, J. M. 2005, MNRAS, 358, 363
Croxall, K. V., Pogge, R. W., Berg, D. A., Skillman, E. D., & Moustakas, J. 2015, ApJ, 808, 42
Croxall, K. V., Pogge, R. W., Berg, D. A., Skillman, E. D., & Moustakas, J. 2016, ApJ, 830, 4
Diaz, A. I., Pagel, B. E. J., & Terlevich, E. 1985, MNRAS, 214, 41P
Diaz, A. I., Terlevich, E., Vilchez, J. M., Pagel, B. E. J., & Edmunds, M. G. 1991, MNRAS, 253, 245
Domgorgen, H. & Mathis, J. S. 1994, ApJ, 428, 647
Eldridge, J. J., Stanway, E. R., Xiao, L., et al. 2017, PASA, 34, e058
Ferland, G. J., Chatzikos, M., Guzmán, F., et al. 2017, Rev. Mexicana Astron. Astrofis., 53, 385
Flores-Fajardo, N., Morisset, C., Stasińska, G., & Binette, L. 2011, MNRAS, 415, 2182
Galarza, V. C., Walterbos, R. A. M., & Braun, R. 1999, AJ, 118, 2775
Haffner, L. M., Dettmar, R. J., Beckman, J. E., et al. 2009, Reviews of Modern Physics, 81, 969
Izotov, Y. I., Thuan, T. X., & Lipovetsky, V. A. 1994, ApJ, 435, 647
Kumari, N., Amorín, R., Pérez-Montero, E., Vílchez, J., & Maiolino, R. 2021, MNRAS, 508, 1084
Lacerda, E. A. D., Cid Fernandes, R., Couto, G. S., et al. 2018, MNRAS, 474, 3727
Law, D. R., Cherinka, B., Yan, R., et al. 2016, AJ, 152, 83
Mannucci, F., Belfiore, F., Curti, M., et al. 2021, MNRAS, 508, 1582
Mateus, A., Sodré, L., Cid Fernandes, R., et al. 2006, MNRAS, 370, 721
Mollá, M., García-Vargas, M. L., & Bressan, A. 2009, MNRAS, 398, 451
Morisset, C. 2004, ApJ, 601, 858
Morisset, C., Delgado-Inglada, G., Sánchez, S. F., et al. 2016, A&A, 594, A37
Pauldrach, A. W. A., Hoffmann, T. L., & Lennon, M. 2001, A&A, 375, 161
Pérez-Montero, E., García-Benito, R., & Vílchez, J. M. 2019, MNRAS, 483, 3322
Pérez-Montero, E., García-Benito, R., Vílchez, J. M., et al. 2016, A&A, 595, A62
Pérez-Montero, E., Kehrig, C., Vílchez, J. M., et al. 2020, A&A, 643, A80
Pérez-Montero, E., Monreal-Ibero, A., Relaño, M., et al. 2014, A&A, 566, A12
Pérez-Montero, E. & Vílchez, J. M. 2009, MNRAS, 400, 1721
Poetrodjojo, H., D'Agostino, J. J., Groves, B., et al. 2019, MNRAS, 487, 79
Rauch, T. 2003, A&A, 403, 709
Reynolds, R. J. 1985, ApJ, 294, 256
Rogers, N. S. J., Skillman, E. D., Pogge, R. W., et al. 2021, ApJ, 915, 21
Vilchez, J. M. & Pagel, B. E. J. 1988, MNRAS, 231, 257
Zhang, K., Yan, R., Bundy, K., et al. 2017, MNRAS, 466, 3217
Zinchenko, I. A., Pilyugin, L. S., Grebel, E. K., Sánchez, S. F., & Vílchez, J. M. 2016, MNRAS, 462, 2715
Zinchenko, I. A., Vílchez, J. M., Pérez-Montero, E., et al. 2021, A&A, 655, A58
Zurita, A., Rozas, M., & Beckman, J. E. 2000, A&A, 363, 9